

PAPER

# Intra- and intercycle interference of angle-resolved electron emission in laser-assisted XUV atomic ionization

To cite this article: A A Gramajo *et al* 2018 *J. Phys. B: At. Mol. Opt. Phys.* **51** 055603

View the [article online](#) for updates and enhancements.

## You may also like

- [Two-photon above-threshold ionization using extreme-ultraviolet harmonic emission from relativistic laser–plasma interaction](#)  
P Heissler, P Tzallas, J M Mikhailova *et al.*
- [High power, high repetition rate laser-based sources for attosecond science](#)  
F J Furch, T Witting, M Osolodkov *et al.*
- [Threshold photoelectron spectroscopy of vibrationally excited nitrogen](#)  
Fabrizio Innocenti, Marie Eypper, Stefano Stranges *et al.*



Easy-to-use and Helium-3 free  
cryogenics solutions

LEARN MORE

# Intra- and intercycle interference of angle-resolved electron emission in laser-assisted XUV atomic ionization

A A Gramajo<sup>1</sup> , R Della Picca<sup>1</sup> , S D López<sup>2</sup> and D G Arbó<sup>2</sup> 

<sup>1</sup>CONICET and Centro Atómico Bariloche (CNEA), 8400 Bariloche, Argentina

<sup>2</sup>Institute of Astronomy and Space Physics IAFE (CONICET-UBA), CC 67, Suc. 28, C1428ZAA, Buenos Aires, Argentina

E-mail: [gramajo.anaalicia@gmail.com](mailto:gramajo.anaalicia@gmail.com) and [diego@iafe.uba.ar](mailto:diego@iafe.uba.ar)

Received 24 November 2017, revised 5 January 2018

Accepted for publication 24 January 2018

Published 13 February 2018



## Abstract

A theoretical study of ionization of the hydrogen atom due to an XUV pulse in the presence of an infrared (IR) laser is presented. Well-established theories are usually used to describe the laser-assisted photoelectron effect: the well-known soft-photon approximation firstly posed by Maquet *et al* (2007 *J. Mod. Opt.* **54** 1847) and Kazansky's theory in (2010 *Phys. Rev. A* **82**, 033420). However, these theories completely fail to predict the electron emission perpendicularly to the polarization direction. Making use of a semiclassical model (SCM), we study the angle-resolved energy distribution of PEs for the case that both fields are linearly polarized in the same direction. We thoroughly analyze and characterize two different emission regions in the angle-energy domain: (i) the parallel-like region with contribution of two classical trajectories per optical cycle and (ii) the perpendicular-like region with contribution of four classical trajectories per optical cycle. We show that our SCM is able to assess the interference patterns of the angle-resolved PE spectrum in the two different mentioned regions. Electron trajectories stemming from different optical laser cycles give rise to angle-independent *intercycle* interferences known as sidebands. These sidebands are modulated by an angle-dependent coarse-grained structure coming from the *intracycle* interference of the electron trajectories born during the same optical cycle. We show the accuracy of our SCM as a function of the time delay between the IR and the XUV pulses and also as a function of the laser intensity by comparing the semiclassical predictions of the angle-resolved PE spectrum with the continuum-distorted wave strong field approximation and the *ab initio* solution of the time-dependent Schrödinger equation.

Supplementary material for this article is available [online](#)

Keywords: angle-resolved photoelectron spectra, laser-assisted photoelectric effect, XUV+IR multiphoton ionization, intra- and intercycle interferences, semiclassical model

(Some figures may appear in colour only in the online journal)

## 1. Introduction

Most experiments on the laser-assisted photoelectric effect (LAPE) combine a fundamental quasimonochromatic laser (infrared, IR) with its high-order harmonic product (XUV and soft-x-ray radiations) acting both on rare-gas atoms [1, 2]. Lately, new sources produced from x-ray free-electron laser in the strong field regime have been used to achieve multiphoton

spectroscopy involving synchronized IR and XUV pulses [3–8]. The photoelectron (PE) spectra from rare-gas atoms have been extensively studied in the simultaneous presence of the two pulses—XUV and IR laser—with a time-controlled delay working as a pump-probe experiment [9–11]. Whereas the first experiments measured the angle-integrated PE emission, only recently simultaneous energy- and angle-resolved PE spectra have been gauged with high degree of resolution [8, 12–17]. The

determination of angle-resolved PE spectra requires state of the art techniques employing several electron time-of-flight analyzers mounted at different angles [8, 15], cold target recoil ion momentum spectroscopy (COLTRIMS) [17] or velocity map imaging (VMI) techniques [13, 14, 16]. Depending on the XUV pulse duration ( $\tau_X$ ), two well-known regimes—sideband and streaking—have been distinguished [16, 18–21]. In the former, where the XUV pulse is longer than the laser period ( $T_L$ ), the PE energy spectrum shows a main line associated with the absorption of one XUV photon accompanied by sideband lines associated with additional exchange of laser photons [2, 12, 22–24]. In the latter, as the XUV pulse is much shorter than the laser wavelength, the electron behaves like a classical particle getting linear momentum from the IR laser field at the instant of ionization [9, 19–21, 25]. The analysis of the resulting two-color PE spectra can provide information about the high-frequency pulse duration, the laser intensity, and the time delay between the two pulses. Moreover, the duration of atomic transitions, like the Auger decay, has been measured with unprecedented levels of accuracy in the attosecond realm [15, 26, 27].

Precise calculations of the response of a rare-gas atom are based on quantum mechanical concepts, i.e., by solving *ab initio* the time-dependent Schrödinger equation (TDSE) for the atomic system in presence of the two pulses within the dipole approximation. The numerical resolution of the TDSE for a multi-electron system relies on the single-active electron approximation with model potentials that reproduce the bound state spectrum of the atom with satisfactory accuracy [28, 29]. Simplified theories are also very useful at the time of understanding the physical processes involved in LAPE. Most of the approximated models of LAPE processes are based on the strong field approximation (SFA) [27, 30, 31]. For example, the broadly used soft-photon approximation (SPA) [32, 33] provides a useful description of some general features in experiments [3, 4, 7, 8, 22, 34]. However, it completely fails to reproduce the measured electron yield from *s*-bound states with high emission angles, predicting no contribution in the direction perpendicular to the polarization axis in LAPE [32, 33, 35, 36], contrarily to TDSE calculations. Besides, the analytic angle-resolved PE spectra derived by Kazansky *et al* [27, 30] and Bivona *et al* [31] are based on simplifications of the temporal integration within the SFA. Following the Bivona *et al* footsteps [31], in previous works we have presented a semiclassical approach that describes the XUV + IR multiphoton ionization with emission parallel and perpendicular to the polarization direction of both fields [37, 38]. Within a one-dimensional semiclassical model (SCM), the PE spectrum was interpreted as the coherent superposition of electron trajectories emitted during the action of the XUV pulse, giving rise to intra- and intercycle interference patterns [39–41]. As far as we know, LAPE ionization has not been studied successfully in detail for arbitrary emission directions. The poor agreement between theoretical and experimental PE angular distributions for the two-color above threshold ionization leads to the necessity of a more comprehensive theoretical description [42, 43].

In this paper we extend the one-dimensional semiclassical approximation (for parallel [37] and perpendicular emission [38]) towards the analysis of the angle-resolved laser-assisted

photoemission spectra of hydrogen atoms by an XUV pulse in the intermediate case between the sideband and streaking regimes, i.e.,  $\tau_X \gtrsim T_L$ . We characterize different regions of the energy-angle plane with different numbers of contributing electron trajectories coherently superimposed to form the interference pattern. Our SCM leads to a simple analytical expression of the doubly differential energy-angle distribution similar to the equation of the diffraction grating in the time domain, giving rise to intercycle interferences (sidebands) modulated by the intracycle pattern (also known as the gross structure [27]). We show that our SCM reproduces the sidebands very accurately (compared to SFA and TDSE computations) for all emission angles, even for directions close to perpendicular emission, where Kazansky's theory [27, 30] and the SPA [32, 33] break down. Besides, we show that the SCM also predicts the downshift of the energy of the continuum states by the ponderomotive energy  $U_p$  due to the average wiggling of the electron driven by the laser field.

The paper is organized as follows. In section 2, we describe the SCM for the case of laser-assisted XUV ionization emphasizing the characterization of the electron trajectory contributions in the different regions of the energy-angle domain. Details of the theoretical calculation are developed in the appendix. In section 3, we present the results and discuss over their comparison with the corresponding calculations within the *ab initio* TDSE and the SFA. Concluding remarks are presented in section 4. Atomic units are used throughout the paper, except when otherwise stated.

## 2. Theory and methods of laser-assisted photoemission

We consider the ionization of an atomic system by the interaction with an extreme ultra violet (XUV) finite laser pulse assisted by an IR laser, both linearly polarized in the same direction  $\mathbf{e}_z$ . In the single-active-electron (SAE) approximation the TDSE reads

$$i\frac{d}{dt}|\psi(t)\rangle = [H_0 + H_{\text{int}}(t)]|\psi(t)\rangle, \quad (1)$$

where  $H_0 = \mathbf{p}^2/2 + V(r)$  is the time-independent atomic Hamiltonian, whose first term corresponds to the electron kinetic energy, and its second term to the electron-core Coulomb interaction. The second term in the right-hand side of equation (1), i.e.,  $H_{\text{int}} = \mathbf{r} \cdot \mathbf{F}_X(t) + \mathbf{r} \cdot \mathbf{F}_L(t)$ , stands for the interaction of the atom with both time-dependent XUV  $[\mathbf{F}_X(t)]$  and IR  $[\mathbf{F}_L(t)]$  electric fields in the length gauge.

As a consequence of the interaction, the bound electron in the initial atomic state  $|\phi_i\rangle$  is emitted with momentum  $\mathbf{k}$  and energy  $E = k^2/2$  into the final unperturbed state  $|\phi_f\rangle$ . The PE momentum distributions can be calculated as

$$\frac{dP}{d\mathbf{k}} = |T_{if}|^2, \quad (2)$$

where  $T_{if}$  is the *T*-matrix element corresponding to the transition  $\phi_i \rightarrow \phi_f$ .

### 2.1. Numerical solution of the TDSE

In order to numerically solve the TDSE in the dipole approximation for the SAE equation (1), we employ the generalized pseudo-spectral method [44–46]. This method combines the discretization of the radial coordinate optimized for the Coulomb singularity with quadrature methods to allow stable long-time evolution using a split-operator representation of the time-evolution operator. Both the bound as well as the unbound parts of the wave function  $|\psi(t)\rangle$  can be accurately represented. Due to the cylindrical symmetry of the system the magnetic quantum number  $m$  is conserved. After the end of the laser pulse the wave function is projected on eigenstates  $|k, \ell\rangle$  of the free atomic Hamiltonian with positive eigenenergy  $E = k^2/2$  and orbital quantum number  $\ell$  to determine the transition amplitude  $T_{if}$  to reach the final state  $|\phi_f\rangle$  (see [47–49]):

$$T_{if} = \frac{1}{\sqrt{4\pi k}} \sum_{\ell} e^{i\delta_{\ell}(p)} \sqrt{2\ell+1} P_{\ell}(\cos\theta) \langle p, \ell | \psi(t_f) \rangle. \quad (3)$$

In equation (3),  $\delta_{\ell}(p)$  is the momentum-dependent atomic phase shift,  $\theta$  is the angle between the electron momentum  $\mathbf{k}$  and the polarization direction  $\mathbf{e}_z$ , and  $P_{\ell}$  is the Legendre polynomial of degree  $\ell$ . In order to avoid unphysical reflections of the wave function at the boundary of the system, the length of the computing box was chosen to be 1200 a.u. ( $\sim 65$  nm) and maximum angular momentum considered was  $\ell_{\max} = 200$ .

### 2.2. Strong field approximation

Within the time-dependent distorted wave theory, the transition amplitude in the prior form and length gauge is expressed as [50, 51]

$$T_{if} = -i \int_{-\infty}^{+\infty} dt \langle \chi_f^-(\mathbf{r}, t) | H_{\text{int}}(\mathbf{r}, t) | \phi_i(\mathbf{r}, t) \rangle, \quad (4)$$

where  $\phi_i(\mathbf{r}, t) = \varphi_i(\mathbf{r})e^{iI_p t}$  is the initial atomic state,  $I_p$  the ionization potential, and  $\chi_f^-(\mathbf{r}, t)$  is the distorted final state. The SFA neglects the Coulomb core-electron interaction in the final channel, therefore we use the well-known Volkov wave function [52] to represent the free electron in the electromagnetic field. The Volkov wave function reads

$$\chi_f^V(\mathbf{r}, t) = (2\pi)^{-3/2} \exp \left[ i(\mathbf{k} + \mathbf{A}(t)) \cdot \mathbf{r} + \frac{i}{2} \int_t^{\infty} dt' (\mathbf{k} + \mathbf{A}(t'))^2 \right], \quad (5)$$

and the vector potential due to the total external field is defined as  $\mathbf{A}(t) = -\int_0^t dt' [\mathbf{F}_X(t') + \mathbf{F}_L(t')]$ . In section 3, we will denote the SFA as the numerical integration of the transition matrix in equation (4) by including the Volkov phase (equation (5)) in the final channel.

### 2.3. Semiclassical model

From TDSE and SFA calculations we have observed that for moderate laser intensities the first and second terms in equation (4) are well separated in the energy domain.

Therefore, with the appropriate choice of the IR and XUV laser parameters considered, we can assume that the energy domain of the LAPE processes is well separated from the IR ionization one. In other words, the contribution of IR ionization is negligible in the energy domain where the absorption of one XUV photon takes place. Furthermore, within the rotating wave approximation we consider the absorption of an XUV photon and neglect the emission of an XUV photon. Thus, the expression of the linearly polarized XUV pulse is reduced to  $\mathbf{F}_X(t) \sim F_{X0}(t)\exp(-i\omega_X t)\mathbf{e}_z/2$ , where  $\omega_X$  is the XUV field frequency. Finally, equation (4) can be written as:

$$T_{if} = -\frac{i}{2} \int_{-\infty}^{+\infty} dt d_z(\mathbf{k} + \mathbf{A}(t)) F_{X0}(t) \exp[iS(t)], \quad (6)$$

where the dipole element  $\mathbf{d}(\mathbf{v})$  is given by

$$\mathbf{d}(\mathbf{v}) = \frac{1}{(2\pi)^{3/2}} \int d\mathbf{r} \exp[-i\mathbf{v} \cdot \mathbf{r}] \mathbf{r} \varphi_i(\mathbf{r}), \quad (7)$$

and the generalized action is

$$S(t) = -\int_t^{\infty} dt' \left[ \frac{(\mathbf{k} + \mathbf{A}(t'))^2}{2} + I_p - \omega_X \right]. \quad (8)$$

As  $\omega_X$  is much higher than the frequency of the IR pulse  $\omega_L$  (and for XUV pulses weaker than the IR laser), we can consider the vector potential as due to the laser field only, neglecting its XUV contribution [21, 37, 38, 50]. Hence the total vector potential can be written as  $\mathbf{A}(t) \simeq \mathbf{A}_L(t) = A_{L0} \sin(\omega_L t) \mathbf{e}_z$  since during the temporal lapse when the XUV pulse is acting, the IR electric field is modeled as a cosine-like wave. Here  $A_{L0} = F_{L0}/\omega_L$  and  $F_{L0}$  is the amplitude of the IR laser field.

For simplicity, we consider a hydrogen atom initially in the ground state and we restrict our analysis to the case where the XUV pulse duration is a multiple of the laser optical cycle, i.e.  $\tau_X = NT_L$  with  $N = 1, 2, \dots$  and  $T_L = 2\pi/\omega_L$ . Since both fields are linearly polarized in  $\mathbf{e}_z$ , we describe the PE momentum in cylindrical coordinates as:  $\mathbf{k} = k_z \mathbf{e}_z + k_{\perp} \mathbf{e}_{\perp}$ .

The SCM approach consists in solving the time integral of equation (6) by means of the saddle-point approximation [53–56]. In this sense, the transition probability can be written as a coherent superposition of the amplitudes of all classical electron trajectories with final momentum  $\mathbf{k}$  over the stationary points  $t_s$  of the generalized action  $S(t)$ :

$$T_{if} = \sum_{t_s} \frac{\sqrt{2\pi} F_{X0}(t_s) d_z(\mathbf{k} + \mathbf{A}_L(t_s))}{|\ddot{S}(t_s)|^{1/2}} \times \exp \left[ iS(t_s) + i\frac{\pi}{4} \text{sgn}[\ddot{S}(t_s)] \right], \quad (9)$$

where  $\ddot{S}(t_s) = -[\mathbf{k} + \mathbf{A}_L(t_s)] \cdot \mathbf{F}_L(t_s)$ ,  $\text{sgn}$  denotes the sign function, and the dipole element from the 1s reads

$$d_z(\mathbf{v}) = -\frac{i2^{7/2}}{\pi} (2I_p)^{5/4} \frac{\mathbf{e}_z \cdot \mathbf{v}}{[\mathbf{v}^2 + 2I_p]^3}. \quad (10)$$

The ionization times  $t_s$  fulfill the equation  $dS(t)/dt|_{t=t_s} = 0$ , i.e.,

$$(k_z + A_L(t))^2 + k_{\perp}^2 = v_0^2, \quad (11)$$

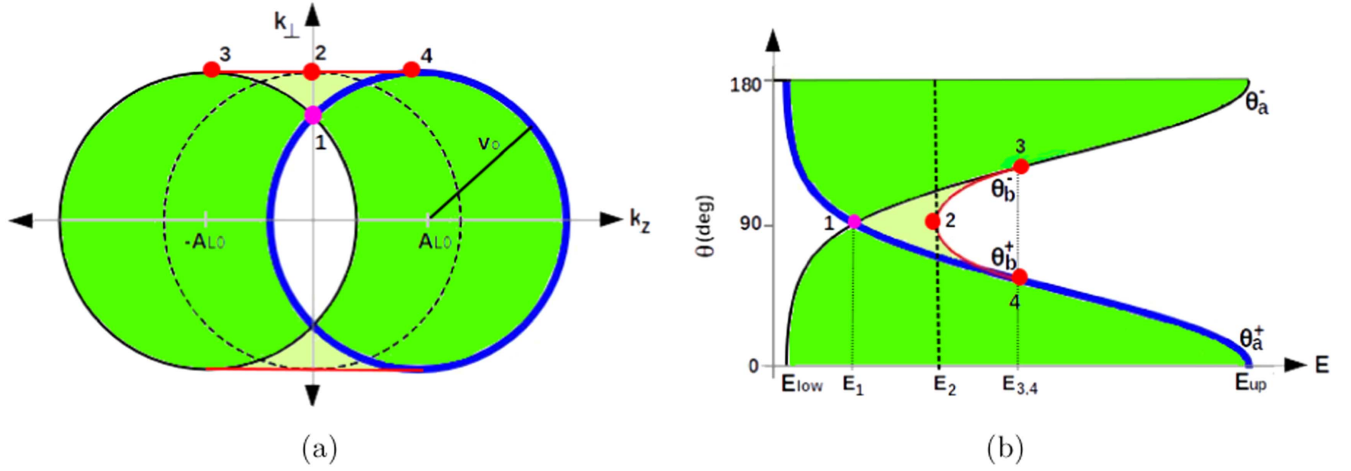


**Figure 1.** (a) Schematic picture for the classically allowed region in the momentum space  $k_z \mathbf{e}_z + k_\perp \mathbf{e}_\perp$ . The dashed–dotted circle of radius  $v_0$  centered at origin represents the main emission line (due to XUV ionization without laser field). As the laser vector potential oscillates, the circle shifts horizontally by  $-A_L(t)$  with amplitude  $A_{L0}$ . In the parallel-like region (green) there are two classical electron trajectories contributing to the probability distribution. In the perpendicular-like region (light green) the number of contributing trajectories is four. The white area represents the classically forbidden region. (b) The same as in (a) but in the energy-angle domain.

where  $v_0 = \sqrt{2(\omega_X - I_p)}$ . In the momentum space the equation (11) is the circumference with center at  $-A_L(t)\mathbf{e}_z$  and radius  $v_0$ . The center position of the circumference oscillates with the time-dependent vector potential. In figure 1(a) we show the representation of equation (11). At time zero the circumference plotted with dashed line is centered at the origin and starts to move to the left as the potential vector increases. When the potential vector reaches the maximal amplitude  $A_{L0}$  the circumference is situated at the left with center at  $-A_{L0}\mathbf{e}_z$ , then it moves to the right. At the end of the IR cycle it returns to the origin. The shaded area indicates the  $\mathbf{k}$  values that were reached by the circumference described by equation (11) at some time during one IR cycle. In other words, the classically allowed momenta are all points of the shaded area for which there exists a time  $t_s$  that verifies equation (11). Outside this domain, ionization times are complex, giving rise to non-classical trajectories with exponentially decaying factors and thus minor relevance compared to real ones. Hereinafter, we restrict our SCM to classically allowed momenta.

In view of the following analysis, we can distinguish two regions in figure 1: the parallel-like region (in green) and the perpendicular-like one (light green) that is delimited by the points 1–4. In each region, the SCM amplitude is derived analogously to previously studied parallel and perpendicular cases [37, 38].

Alternatively, these regions can be also identified in the energy-angle plane via the transformation  $(k_z, k_\perp) \rightarrow (E, \theta)$ , with  $E = (k_z^2 + k_\perp^2)/2$  and  $\tan \theta = k_\perp/k_z$  (see figure 1(b)). In this plane, the curves delimiting the allowed regions are defined by

$$\theta_a^\pm(E) = \arccos\left(\pm \frac{E + A_{L0}^2/2 - v_0^2/2}{\sqrt{2E}A_{L0}}\right), \quad (12)$$

$$\theta_b^\pm(E) = \arcsin\left(\pm \frac{v_0}{\sqrt{2E}}\right) + \frac{(1 \mp 1)\pi}{2}, \quad (13)$$

which, in momentum space, correspond to the circles in thick blue, thin black lines and the connecting points 3 and 4 in thin red (gray) line, respectively. The lower and upper classical values for the electron energy are  $\theta$  dependent. For example, in the forward and perpendicular emission cases ( $\theta = 0^\circ$  and  $90^\circ$  respectively), these values are  $E_{\text{low,up}} = (v_0 \mp A_{L0})^2/2$  and  $E_1 = (v_0^2 - A_{L0}^2)/2$ ,  $E_2 = v_0^2/2$  for the perpendicular emission case, in agreement with previous works [37, 38].

The deduction of the analytical expressions for the ionization times  $t_s$  that fulfill equation (11) is detailed in the appendix. After the algebra guided in the appendix, it can be shown that the emission probability (equation (9)) is

$$|T_{\text{if}}|^2 = 4\Gamma(k_\perp)F(\mathbf{k})B(k), \quad (14)$$

where

$$B(k) = \frac{\sin^2(N\tilde{S}/2)}{\sin^2(\tilde{S}/2)}, \quad (15)$$

$$\tilde{S} = (2\pi/\omega_L)(E + I_p + U_p - \omega_X), \quad (16)$$

and the *intracycle* factor is

$$F(\mathbf{k}) = \left| f_+(\mathbf{k}) \cos\left(\frac{\Delta S_+}{2} + \frac{\pi}{4} \text{sgn}[\beta_+(\mathbf{k})]\right) - \Theta\left(1 + \frac{\beta_-}{A_{L0}}\right) f_-(\mathbf{k}) \cos\left(\frac{\Delta S_-}{2} - \frac{\pi}{4} \text{sgn}[\beta_-(\mathbf{k})]\right) \right|^2, \quad (17)$$

where  $\beta_\pm(\mathbf{k})$ ,  $f_\pm(\mathbf{k})$  and  $\Delta S_\pm$  are defined in equations (25), (32) and (31) of the appendix, respectively, and  $\Theta$  is the Heaviside function. The ionization rate  $\Gamma(k_\perp)$  in equation (14) is identical for all subsequent ionization trajectories which depend on the perpendicular component of the final momenta  $k_\perp$ , i.e.,

$$\Gamma(k_\perp) = \frac{4F_{X0}^2}{\pi F_{L0}\omega_X^6} \sqrt{v_0^2 - k_\perp^2}. \quad (18)$$



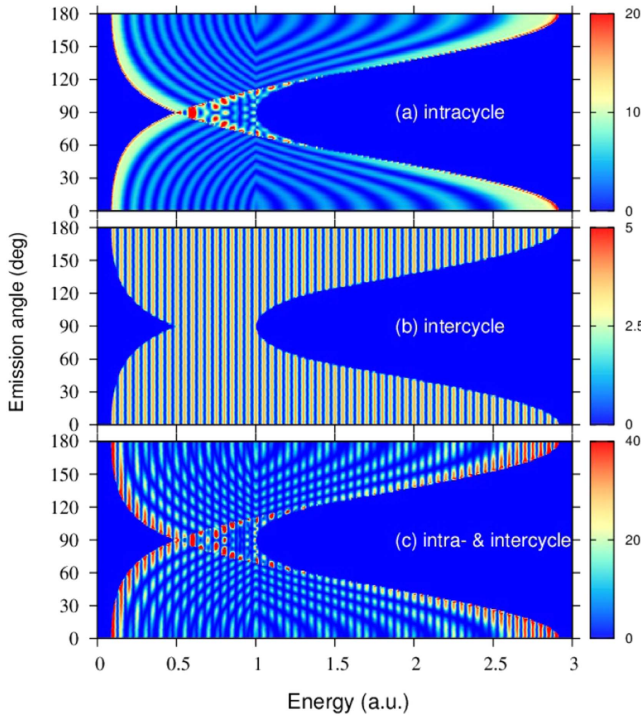


**Figure 2.** (a) SCM intracycle factor  $F(\mathbf{k})$ , (b) SCM intercycle interference factor  $B(k)$  considering  $N = 2$  optical cycles, and (c) the product  $F(\mathbf{k})B(k)$  showing the interplay of inter- and intracycle interferences. The IR and XUV laser parameters are  $\omega_L = F_{L0} = F_{X0} = 0.05$  a.u. and  $\omega_X = 1.5$  a.u.

The equation (14) indicates that the PE spectrum can be factorized in two different contributions: (i) the *intracycle interference* stemming from trajectories within the same cycle governed by factor  $F(\mathbf{k})$ , and (ii) the *intercycle interference* stemming from trajectories released at different cycles, resulting in the well-known sidebands given by factor  $B(k)$ . The latter factor is periodic in the final PE energy with peaks at positions

$$E_n = \omega_X + n\omega_L - I_p - U_p, \quad (19)$$

where  $n = 0, \pm 1, \pm 2, \dots$  is interpreted as the number of IR photons absorbed ( $n > 0$ ) or emitted ( $n < 0$ ), added to the absorption of one XUV photon and downshifted by the ponderomotive energy  $U_p$ . When the duration of the pulses extends infinitely we have  $B(k) \rightarrow \sum_n \delta(E - E_n)$ , which stands for the conservation of energy.

In figure 2, we show the respective contributions of intra- and intercycle factors,  $F(\mathbf{k})$  and  $B(k)$ , to the SCM emission probability in equation (14) for a XUV pulse duration of  $2T_L$ . In figure 2(a) we present the intracycle factor  $F(\mathbf{k})$  that depends on both PE energy and angle. We see that this factor has a richer structure in the perpendicular-like region (four contributing electron trajectories) than in the parallel-like region (two contributing trajectories). Furthermore, equation (17) predicts a jump due to the discontinuity of the sign function. Since the sign of  $\beta_-(\mathbf{k})$  is constant throughout the domain, we only expect a discontinuity in the intracycle factor at  $\beta_+ = 0$  (when its sign changes), that can be recognized in the figure at  $E_{\text{disc}} = v_0^2/2 = 1$  independently of the emission angle. In the

next section we analyze this discontinuity as a function of the beginning time of the XUV pulse.

In figure 2(b) we plot the intercycle factor  $B(k)$  in the classical domain, we observe the periodic stripes separated by  $\omega_L$  at energies  $E_n$  according to equation (19). Finally, when both intra- and intercycle factors are multiplied, we obtain the spectra plotted in figure 2(c). We observe that the intracycle interference pattern works as a modulation of the intercycle interference pattern. The agreement between the present semiclassical description and the ones obtained by SFA and TDSE is discussed in the next section.

Finally, it is interesting to note that the present angle-dependent SCM formalism comprises the forward and perpendicular emission as particular cases, which were already analyzed in our previous works [37, 38]. In fact, when the electron emission is parallel to both laser fields ( $k_\perp = 0$ ), the second term inside the square modulus of  $F(\mathbf{k})$  (equation (17)) is null and, thus, equation (14) becomes equation (23) of [37]. On the other hand, in the perpendicular electron emission case ( $k_z = 0$ ) we have that  $\beta_- = -\beta_+$  and then  $\Delta S_- = \Delta S_+ \equiv \Delta S$ . Thus the expression (17) can be rewritten as (see also equation (18) of [38])

$$F(\mathbf{k}) = \frac{4}{\sqrt{1 - \beta_-^2/A_{L0}^2}} \underbrace{\cos^2\left(\frac{\Delta S}{2} + \frac{\pi}{4}\right)}_{\text{intra-half-cycle}} \sin^2\left(\frac{\tilde{S}}{4}\right), \quad (20)$$

which can be understood as the contribution of an intra-half-cycle factor and  $\sin^2(\tilde{S}/4)$  that interferes destructively for the absorption and/or emission of an even number of IR photons, which leads to the exchange of only an odd number of laser photons in the formation of the sidebands. This fact can be observed in figure 2(c) where even sideband peaks are canceled at  $\theta = 90^\circ$ .

### 3. Results and discussion

In the following, we analyze the angle-resolved PE spectrum

$$\frac{d^2P}{\sin\theta dE d\theta} = 2\pi\sqrt{2E}|T_{\text{if}}|^2 \quad (21)$$

and compare the outcome of the SCM with quantum calculations within the SFA [27, 30, 31, 39, 40, 57] and by solving the TDSE [44–46]. We model the XUV and IR laser pulses as

$$\mathbf{F}_i(t) = F_{i0}(t - t_{ib}) \cos\left[\omega_i\left(t - \Delta_i - \frac{\tau_i}{2}\right)\right] \mathbf{e}_z, \quad (22)$$

where  $i = L$  and  $X$  denotes the IR laser and XUV pulses, respectively. The envelopes of the electric fields in equation (22) were chosen with a trapezoidal shape comprising one-cycle ramp on and one-cycle ramp off, i.e.,

$$F_{i0}(t) = F_{i0} \begin{cases} t/T_i & \text{if } 0 \leq t \leq T_i \\ 1 & \text{if } T_i \leq t \leq \tau_i - T_i \\ (\tau_i - t)/T_i & \text{if } \tau_i - T_i \leq t \leq \tau_i \end{cases}$$

and zero otherwise, where  $T_i = 2\pi/\omega_i$  and  $\tau_i$  are the  $i$ -field period and pulse duration, respectively. For the sake of

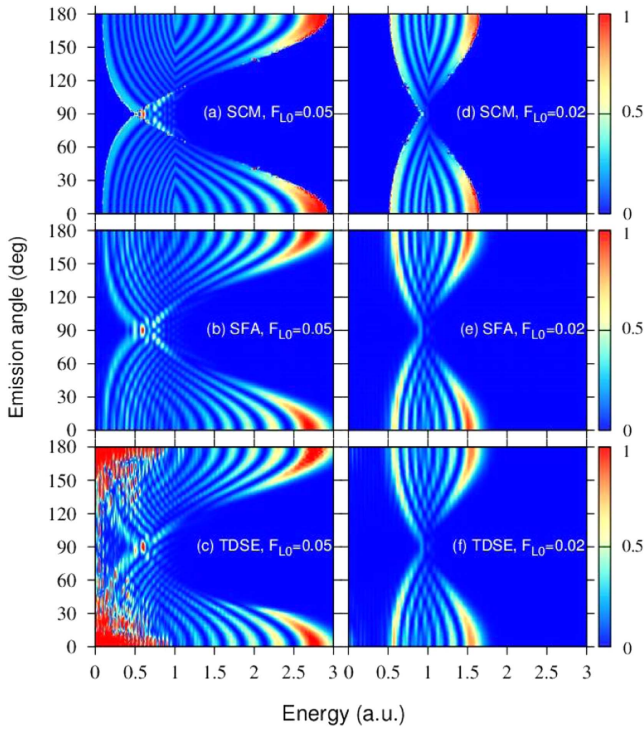


**Figure 3.** Angle-resolved photoelectron spectra in arbitrary units for an XUV pulse duration of  $\tau_X = T_L$  and time delay  $\Delta_X = 0$ , calculated at different laser peak fields ( $F_{L0} = 0.05$  a.u. in (a)–(c), and  $F_{L0} = 0.02$  a.u. in (d)–(f)) within the SCM ((a) and (d)), the SFA ((b) and (e)) and the TDSE ((c) and (f)). The IR laser frequency is  $\omega_L = 0.05$  a.u. and the XUV pulse parameters are  $\omega_X = 1.5$  a.u. and  $F_{X0} = 0.05$  a.u.

simplicity, we suppose that the duration of both laser fields comprises integer number of cycles, i.e.,  $\tau_i = N_i T_i$  where  $N_i$  is a natural number. We choose the origin of the time scale as the beginning of the IR laser pulse, i.e.,  $t_{Lb} = 0$ , with no displacement of it  $\Delta_L = 0$ , so that the IR laser field is a cosine-like pulse centered in the middle of the pulse. The beginning time of the XUV pulse  $t_{Xb} = \Delta_X + \tau_L/2 - \tau_X/2$  marks the starting time of the active window for LAPE, that corresponds to the temporal interval  $[t_{Xb}, t_{Xb} + \tau_X]$  when both pulses are superimposed.

Hereinafter, in our calculations we use the IR and XUV pulses with frequencies as  $\omega_L = 0.05$  and  $\omega_X = 30\omega_L = 1.5$ , respectively, and laser duration  $\tau_L = 5T_L$ . In addition, the XUV duration is an integer of the laser period, i.e.  $\tau_X = NT_L$ . In figure 2(a) we have plotted the intracycle factor (equation (17)) that is related to the angle-resolved PE spectrum considering an XUV pulse of duration  $\tau_X = T_L$ , i.e.  $N = 1$ , with peak amplitude  $F_{X0} = 0.05$  and  $\Delta_X = 0$ . In figure 3, we show results for the ionization probability distribution for  $F_{L0} = 0.05$  in the left column ((a)–(c)) and  $F_{L0} = 0.02$  in the right column ((d)–(f)). We see that the SCM electron yield (figure 3(a)) is fully explained by the intracycle interference factor  $F(\mathbf{k})$  (figure 2(a)); the only difference between figures 2(a) and 3(a) is that in the latter the momentum distribution includes factor  $8\pi k\Gamma(k_L)$  (see equations (21) and (14)). In the second row ((b) and (e)), we show results of the SFA and in the third row ((c) and (f)), the

corresponding numerical solution of the TDSE. Due to the close agreement between the SCM and the SFA with the TDSE angle-resolved energy distributions, one may conclude that the effect of the Coulomb potential on the energy spectrum is very small if not negligible. However, the analysis of the effect of the Coulomb potential of the remaining core on the electron yield deserves a thorough study, which is beyond the scope of this paper.

For the laser and XUV parameters used in the left column of figure 3, the lower and upper classical boundaries of the energy distributions in the direction along the polarization axis ( $\theta = 0^\circ$  and  $\theta = 180^\circ$ ) are  $(v_0 - F_{L0}/\omega_L)^2/2 \simeq 0.086$  and  $(v_0 + F_{L0}/\omega_L)^2/2 \simeq 2.91$ , respectively [37]. The enhancement of the probability distribution near threshold in the TDSE calculation in figure 3(c) is due to ATI ionization by the laser field (with no XUV pulse). This contribution is highly suppressed in the SFA calculations [57] in figure 3(b) and completely neglected in our SCM in figure 3(a). For emission perpendicular to the polarization direction ( $\theta = 90^\circ$ ), the lower and upper classical boundaries (first column of figure 3) are  $[v_0^2 - (F_{L0}/\omega_L)^2]/2 = 0.5$  and  $v_0^2/2 = 1$ , respectively, for the case that  $F_{L0} = 0.05$  [38]. We see that the quantum SFA and TDSE results circumscribe to the classical boundaries, except for a thin (in energy domain) decaying probability beyond the classical boundaries. As shown in section 2, the SCM predicts a discontinuity of the intracycle stripes which, in the case of figure 3, is set at  $E_{\text{dis}} = v_0^2/2 = 1$ , as is clearly observed in figures 3(a) and (d). The intracycle stripes for forward emission ( $\theta < 90^\circ$ ) have positive slope at the left of the discontinuity ( $E < E_{\text{dis}} = 1$ ), whereas they have negative slope at the right of it ( $E > E_{\text{dis}} = 1$ ) in figures 3(a) and (d); and the opposite behavior for backward emission ( $\theta > 90^\circ$ ). We observe that such discontinuity is blurred in the quantum SFA and TDSE calculations, where the two kinds of intracycle stripes (with positive and negative slope) coexist in an energy region close to  $E_{\text{dis}}$ .

In order to study the dependence of the angle-resolved PE spectrum with the laser intensity, we show in the right column of figure 3 the results using a laser peak field of  $F_{L0} = 0.02$ . As the laser intensity is lower than the one used in the first column, the classically allowed region shrinks. In particular, the energy distribution along the polarization axis is bounded by the lower  $(v_0 - F_{L0}/\omega_L)^2/2 \simeq 0.51$  and upper  $(v_0 + F_{L0}/\omega_L)^2/2 \simeq 1.64$  classical limits [37]. In turn, the classical boundaries for emission perpendicular to the polarization axis are  $[v_0^2 - (F_{L0}/\omega_L)^2]/2 \simeq 0.92$  and  $v_0^2/2 = 1$ , being the last one insensitive to the laser intensity [38]. From figures 3(a) and (b) we observe that the number of intracycle stripes diminishes as the laser intensity decreases. For the TDSE calculations in figure 3(f), we observe a much lower contribution from near-threshold ATI by the laser compared to figure 3(c) since the intensity of the laser in the latter is only the 16% of what corresponds to the former. From a direct comparison between the angle-resolved PE spectra for different laser intensities, we can conclude that they can be very useful at the time of experimentally determining the elusive magnitude of the laser intensity.

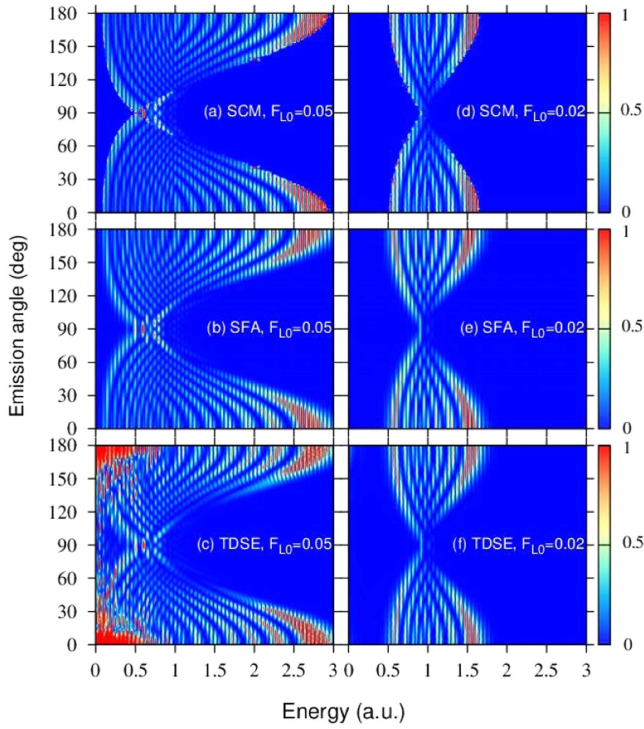


**Figure 4.** Angle-resolved photoelectron spectra in arbitrary units for an XUV pulse duration of  $\tau_X = 2T_L$  and time delay  $\Delta_X = 0$ , calculated at different laser peak fields ( $F_{L0} = 0.05$  a.u. in (a)–(c), and  $F_{L0} = 0.02$  a.u. in (d)–(f)) within the SCM ((a) and (d)), the SFA ((b) and (e)) and the TDSE ((c) and (f)). The IR laser frequency is  $\omega_L = 0.05$  a.u. and the XUV pulse parameters are  $\omega_X = 1.5$  a.u. and  $F_{X0} = 0.05$  a.u.

As explained in section 2, for an XUV pulse of a duration longer than the laser period, intercycle interferences give rise to the formation of sidebands. We clearly see the sideband formation in figure 4, where the duration of the XUV pulse involves two optical cycles, i.e.,  $\tau_X = 2T_L$ . The rest of the parameters are the same as in figure 3. In general, we observe that the domain of the angle-resolved energy distribution is independent of the XUV pulse duration ( $\tau_X \geq T_L$ ) (the same as in figure 3). The only difference between the angle-resolved PE spectra of figures 3 and 4 is the formation of the sidebands, here depicted as vertical isoenergetic lines at energy values  $E_n$  according to equation (19) and separated by the photon energy  $\omega_L = 0.05$ . We see that the sidebands, stemming from the coherent superposition of the contributing trajectories at the two different optical cycles, are modulated by the intracycle pattern of figure 3, due to the contributing trajectories within the same optical pulse. So far, we have seen that the SCM and SFA predicted backward–forward symmetrical emission, i.e.,  $\theta \leftrightarrow \pi - \theta$  (see figures 3(a), (b), (d), (e) and 4(a), (b), (d), and (e)). This symmetry holds approximately, but it is not accurate in the TDSE calculations. There are two reasons for the backward–forward symmetry breaking: the effect of the Coulomb potential of the remaining ion and the depletion of the ground state [21, 57–59]. These two effects are completely neglected within the SFA and, therefore, also within the SCM.

Another way of breaking the forward–backward symmetry is by including a time delay  $\Delta_X$  with respect to the hitherto XUV beginning time  $\tau_L/2 - \tau_X/2$  for the case of the two co-centered pulses. For the sake of comparison, let us define the module  $2\pi$  optical phase as the phase of the starting time of the XUV pulse with respect to the vector potential  $\mathbf{A}(t)$  as<sup>3</sup>

$$\phi \equiv \omega_L t_{Xb} = \omega_L \Delta_X + (N_L - N)\pi, \quad (23)$$

where  $\phi$  is restricted to  $0 \leq \phi < 2\pi$ . By varying  $\Delta_X$  in equation (22), the optical phase  $\phi$  defined in equation (23) changes accordingly. Whereas the active window for XUV ionization shifts in the time domain, the vector potential of the laser pulse changes its shape relative to the active window, with an ensuing change of shape of the intracycle interference pattern. In figure 5, we observe how the intracycle interference pattern (angle-resolved PE spectrum for  $\tau_X = T_L$ ) changes when the optical phase varies, i.e.,  $\phi = \pi/2, \pi$ , and  $3\pi/2$ , for the left ((a)–(c)), middle ((d)–(f)), and right ((g)–(i)) columns, respectively. In figures 5(a), (d), and (g) the SCM exhibits the change of the intracycle interference pattern with  $\phi$ . For the optical phase  $\phi = \pi$  in figure 5(d) the active window is shifted by half laser period with respect of the optical phase  $\phi = 0$  in figure 3(d) and, thus, the vector potential relative to the active window inverts (it changes sign). Therefore, we should expect a forward–backward inversion of the angle-resolved spectrum. Moreover, due to its forward–backward symmetry, the electron emission stays unaltered. The forward–backward inversion can be observed by comparing figures 5(g) and (a) since the change of the optical phase is  $\pi$  (equation (23)). We note that, similarly to the  $\phi = 0$  case, the aforementioned discontinuity occurs at  $E_{\text{dis}} = 1$  in figure 5(d). Nevertheless, for the general case, the line of discontinuity depends on  $\phi$  (through  $t_{Xb}$ ) and the emission angle; in fact, it is possible to deduce that the energy values where the discontinuity takes place follow

$$E_{\text{dis}}(t_{Xb}, \theta) = \frac{1}{2} \left[ \sqrt{v_0^2 - A_L^2(t_{Xb}) \sin^2 \theta} - A_L(t_{Xb}) \cos \theta \right]^2. \quad (24)$$

This equation generalizes the discontinuity previously deduced for forward and perpendicular cases [37, 38]. For  $\phi = 0$  and  $\phi = \pi$ ,  $E_{\text{dis}} = v_0^2/2 = 1$  a.u., which is independent of the emission angle  $\theta$ . For  $\phi = \pi/2$ , in figure 5(a), the discontinuity has displaced to one classical boundary in equation (24), whereas for  $\phi = 3\pi/2$ , figure 5(g), the discontinuity coincides with the other classical boundary in equation (24), losing its entity in both cases. In the supplemental material, we show a video available online at [stacks.iop.org/JPB/51/055603/mmedia](https://stacks.iop.org/JPB/51/055603/mmedia) of how the SCM angle-resolved PE spectrum changes with the optical phase for a larger number of optical phases than the ones depicted in figure 5. There it is easy to observe the angle dependence of  $E_{\text{dis}}$ . The SFA and TDSE angle-energy distributions in the respective figures 5(e) and (f) blur the mentioned discontinuity as previously discussed for  $\phi = 0$ . It is worth

<sup>3</sup> Here the  $2\pi$ -equivalence  $a \equiv b$  means that  $(a-b)/2\pi$  is integer.



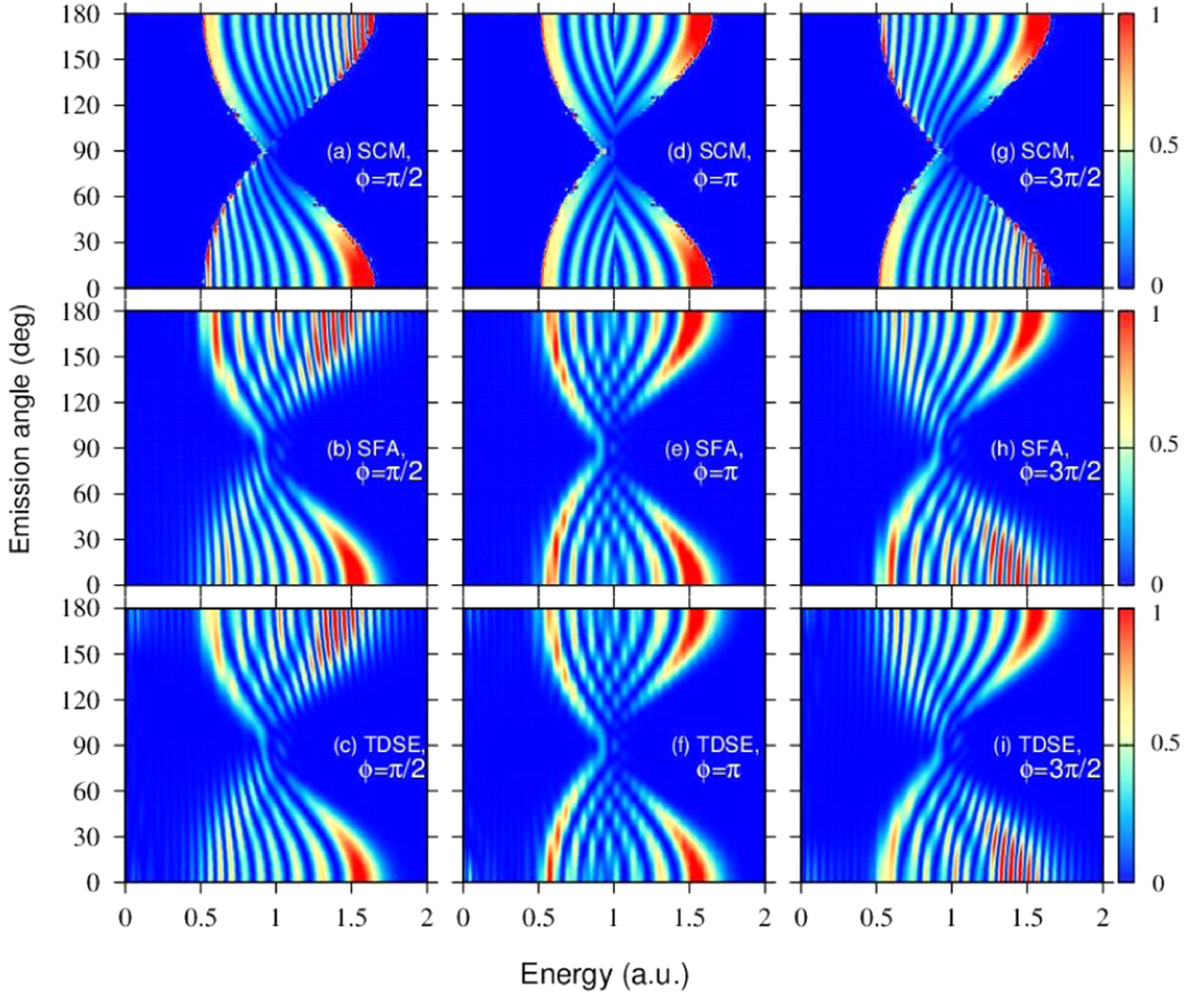


**Figure 5.** Angle-resolved photoelectron spectra in arbitrary units for an XUV pulse duration of  $\tau_X = T_L$  calculated at different optical phases ( $\phi = \pi/2$  in (a)–(c),  $\pi$  in (d)–(f), and  $3\pi/2$  in (g)–(i)) within the SCM ((a), (d) and (g)), the SFA ((b), (e) and (h)) and the TDSE ((c), (f) and (i)).  $F_{X0} = \omega_L = 0.05$  a.u.,  $\omega_X = 1.5$  a.u. and  $F_{L0} = 0.02$  a.u.

mentioning that the SCM resembles SFA and TDSE angle-resolved PE distributions quite accurately for all optical phases.

In order to study the formations of sidebands for different optical phases  $\phi$ , in figure 6 we plot the angle-resolved PE spectrum for the same XUV and laser parameters as in figure 5 except that the XUV pulse duration is  $\tau_X = 2T_L$ . We see the presence of the sidebands produced by the intercycle interference between the contributions of the photoemission within the first and second optical cycles. As shown before, sidebands (the intercycle pattern) are modulated by the intracycle pattern of figure 5. As explained in the last paragraph, we see that the energy-resolved PE spectrum is exactly symmetric when calculated for  $\phi = \pi$  within the SCM (figure 6(d)) and the SFA (figure 6(e)), and approximately symmetric when calculated within the TDSE. Besides, we see that the asymmetry observed in the intracycle interference for optical phase  $\phi = \pi/2$  ((a)–(c)) and  $3\pi/2$  ((g)–(i)) is strongly suppressed in

the respective figures 6(a)–(c) and figures 6(g)–(i) compared to figure 5, due to the presence of the intercycle interference in the former. We see that the dependence of the PE spectra on the delay diminishes as the XUV duration increases. In fact, in the limit of infinite durations, the sidebands are represented as delta functions in the energy domain, i.e.,  $\delta(E - E_n)$  where  $E_n$  is given by equation (19), independently of the XUV delay in agreement with the SPA.

The SPA has been widely employed to depict satisfactorily experimental results [7, 22, 60–63]. However, since its dipole element involved is proportional to  $\mathbf{e}_z \cdot \mathbf{k} = k_z$ , the SPA predicts no emission in the direction perpendicular to the polarization axis of the laser field [32, 33]. For that reason, in order to compare the emission yield in the perpendicular direction for different theories, we focus on the intracycle interference pattern in the perpendicular-like region. Figures 7(a)–(d) are an augmentation of the angle-resolved PE spectrum near the perpendicular-like region for the same

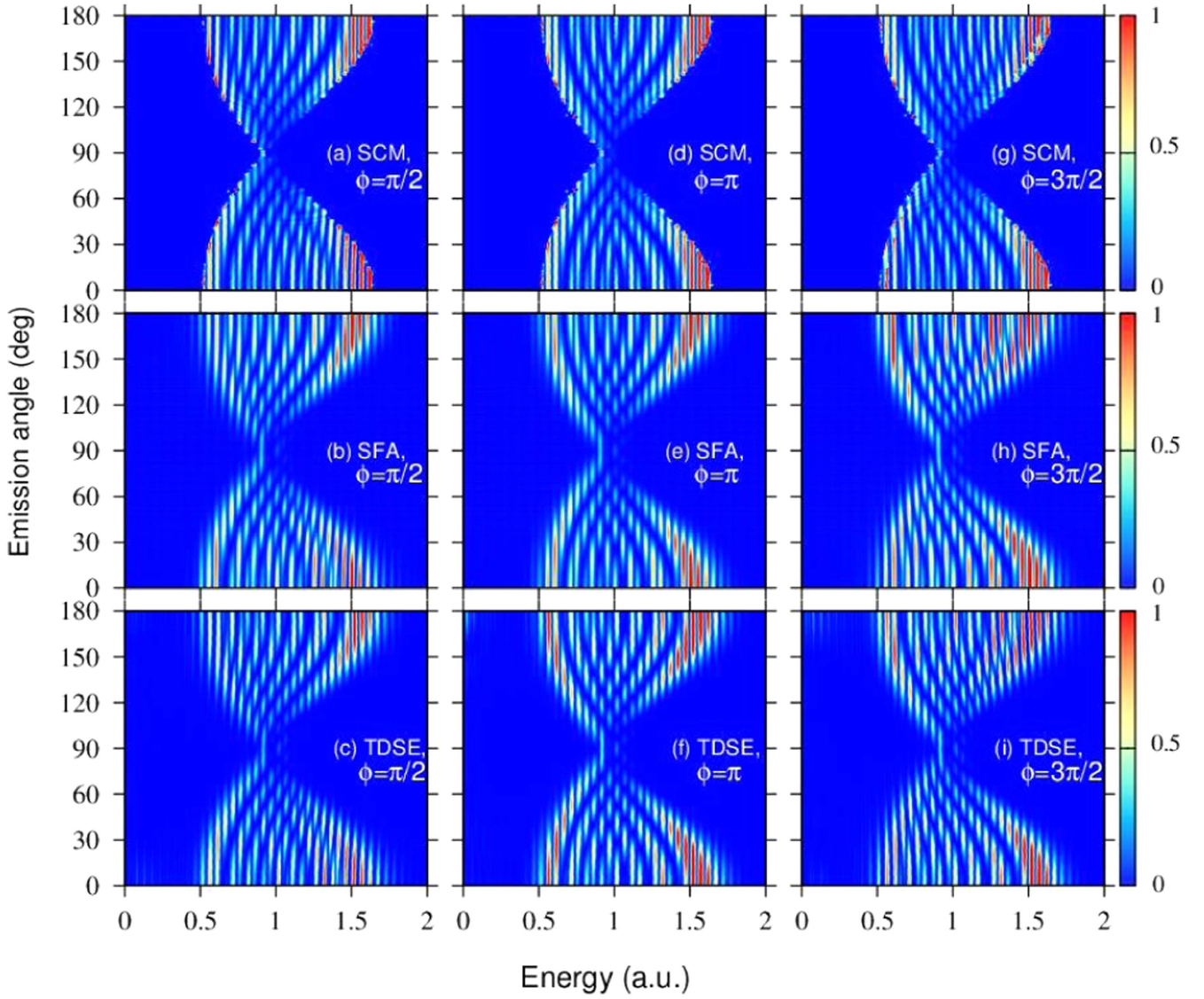


**Figure 6.** Angle-resolved photoelectron spectra in arbitrary units for an XUV pulse duration of  $\tau_X = 2T_L$  calculated at different optical phases ( $\phi = \pi/2$  in (a)–(c),  $\pi$  in (d)–(f), and  $3\pi/2$  in (g)–(i)) within the SCM ((a), (d) and (g)), the SFA ((b), (e) and (h)) and the TDSE ((c), (f) and (i)). The IR laser parameters are the same as in figure 5.

XUV and laser parameters used hitherto for the high laser intensity, i.e.,  $F_{L0} = 0.05$  and  $\tau_X = T_L$  in figure 3. Here we note that the SPA predicts discrete final energy values according to the sideband values, since it is derived for infinitely long pulses (see for example equation (2.10) of [33]). Not only have we included the ponderomotive shift, so that the sideband positions are in agreement with the energy conservation equation (19), but we have also extended it linearly for continuous energy values for better comparison with other theories. In this way, the SPA can be interpreted as the modulator of the sidebands, i.e. the intracycle pattern. We observe a qualitative agreement among the SCM (b), SFA (c), and TDSE (d) distributions, as discussed previously. However, the SPA model (figure 7(a)) is shifted towards higher energy values. More importantly, the SPA exhibits null electron perpendicular emission, according to [33]. The TDSE angle-resolved PE spectrum shows some degree of forward–backward asymmetry since the Coulomb force of the

remaining core cannot be neglected. This fact can be easily understood since the force of the electric field is weak (and vanishes in the perpendicular direction) and, therefore, the main hypothesis of the SFA fails close to perpendicular emission ( $\theta \sim 90^\circ$ ).

As observed in figure 3, the emission is highly dependent on the laser intensity. Because of this, it is worth to analyze the contribution of the ionization probability in the perpendicular direction for different intensities. In what follows, we compute the total ionization probability at a fixed emission angle, integrating in energy the PE spectrum equation (21). In figure 8 we present the ratio of perpendicular and forward emission, i.e.,  $P_\perp/P_\parallel$ , as a function of the laser electric field amplitude  $F_{L0}$  within the SCM, the SFA and the TDSE approaches. We have considered fixed  $F_{X0} = 0.05$ . Since the SFA and SCM probabilities are proportional to the XUV intensity, we expect the result not to change for different values of  $F_{X0}$ . As we have observed before in figure 3, the TDSE spectra show a high



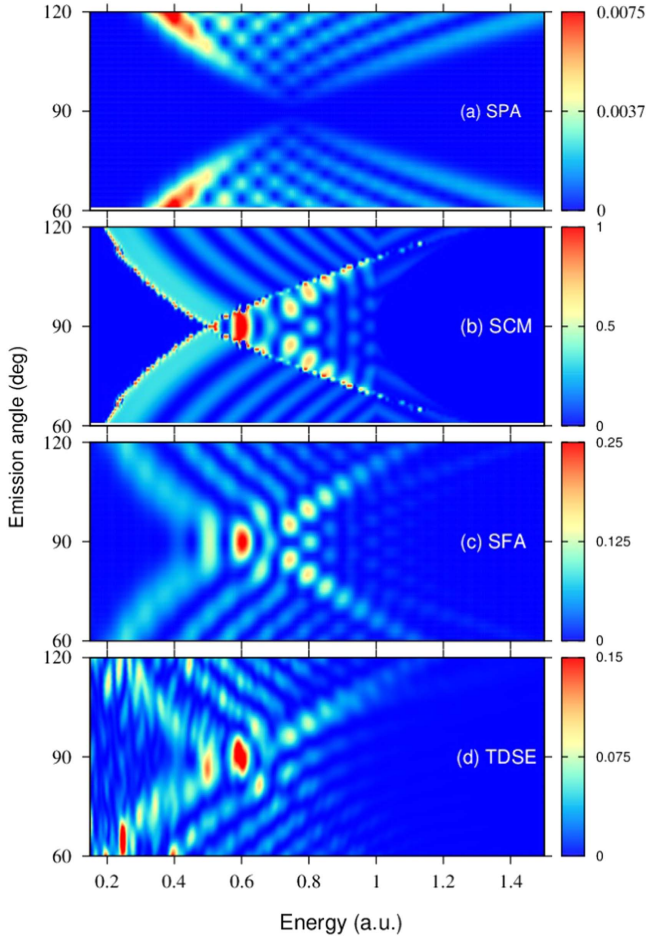


**Figure 7.** Angle-resolved PE spectra in arbitrary units in the perpendicular-like region for an XUV pulse duration of  $\tau_X = T_L$  calculated within the SPA (a), the SCM (b), the SFA (c), and the TDSE (d). The IR laser parameters are the same as in the figure 3 and  $F_{L0} = 0.05$  a.u.

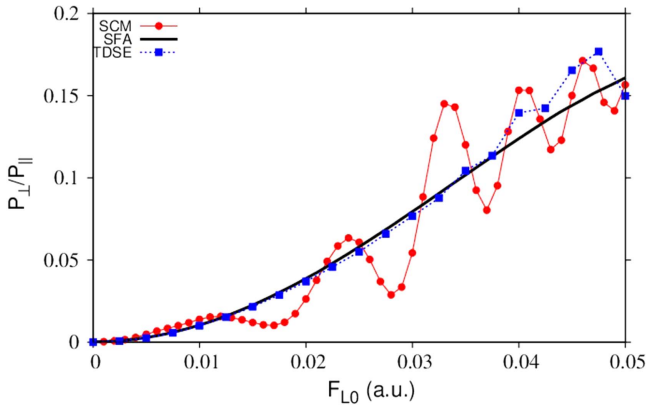


**Figure 8.** Ratio of transversal and forward total emission probabilities as function of the laser amplitude within the SCM (red solid line with circles), the SFA (black solid line) and the TDSE (blue dashed line with squares).

emission probability at low energies due to the ATI ionization by the IR pulse alone. Therefore, in order to compute the TDSE total ionization probability at  $\theta = 0^\circ$ , we have omitted the contribution of direct ionization probability, i.e.

$P_{\parallel} \simeq P_{\parallel}^{\text{XUV+IR}} - P_{\parallel}^{\text{IR}}$ . Then, the TDSE ratio becomes very sensitive to this straightforward estimation of  $P_{\parallel}$ , especially for  $F_{L0} \geq 0.04$ , as we can observe in figure 8. The three theories predict that  $P_{\perp}/P_{\parallel}$  increase with the laser amplitude, showing that for higher laser intensities the perpendicular emission becomes significant and cannot be neglected. The SCM ratio shows oscillations around the quantum calculations (TDSE and SFA), which are related to the abrupt cut in the energy domain due to the classical boundaries.

The last point we want to discuss is the possibility of extending the present model to many-electron atoms and molecules [50, 64–66]. In our simple SAE case, the differential ionization probability is factorized (see equation (14)) so that the temporal interference is separated and common to all atomic species. We mean that the dipole element  $\mathbf{d}(\mathbf{k} + \mathbf{A}_L(t_s))$  has all the information of the atomic system (except for the ionization potential that is also contained in the intercycle factor). In order to extend our model for the case of multielectronic atoms and molecules, besides the temporal intra- and intercycle interference we should consider spatial interference due to action of the rest of the electrons or emission from the several nuclei of the molecule laying in the (much more complicated) atomic or molecular dipole element. A similar approach has been considered for laser ionization of  $\text{H}_2^+$  [50, 65] and Argon [64] obtaining good agreement with experimental data.

#### 4. Conclusions

We have studied the electron spectrum at all emission angles produced by atomic hydrogen initially in the ground state subject to an XUV pulse in the presence of an infrared laser pulse. We have generalized the SCM previously posed to study LAPE in the direction along the polarization axis [37] and perpendicularly to it [38]. The classically allowed angle-energy domain can be divided in two different regions: the parallel-like and the perpendicular-like regions. In the former, two classical electron trajectories per optical cycle contribute to the (intracycle) interference pattern which modulates the sidebands stemming from the (intercycle) interference of the electron trajectories at different optical cycles. In the latter, the four contributing classical electron trajectories can be grouped in two pairs in one optical cycle, giving rise to a grosser (intrahalfcycle) structure which modulates the intracycle pattern. We have shown that, as the laser intensity increases, the angle-resolved PE spectra become wider in the energy domain showing a considerable extended perpendicular-like region bound within the classical domain. We have observed a very good agreement between the SCM angle-resolved energy spectrum with the corresponding SFA and the *ab initio* calculations of the TDSE. The relevance of the SCM is evident for emission in the perpendicular-like region. Whereas the SPA [32, 33] and Kazansky's first-order time-dependent perturbation theory [27, 30, 67, 68] predict null perpendicular emission for ionization from an *s* state, our SCM foresees appreciable non-zero probability in the perpendicular-like region in the line of Bivona's theory [31]

and in agreement with SFA and TDSE calculations. The TDSE emission yield experiences a breaking of the forward–backward symmetry for short XUV pulses, which is mostly recovered as the XUV pulse duration comprises a few laser optical cycles. Finally, we have analyzed the angle-resolved electron spectrum for different time delays  $\Delta_X$  between the two pulses. We have also shown that when the XUV pulse duration is a multiple of the laser period and for optical phases  $\phi = 0$ , and  $\pi$ , the emission within the TDSE is highly symmetrical in the forward and backward direction, in agreement with the SFA and SCM forward–backward. Forward–backward asymmetries come up for optical phases different from  $\phi = 0$  and  $\pi$ . In particular, the angle-resolved PE spectra become accessible using, for example, VMI spectrometer or COLTRIMS technique with long term stability of the synchronization between the XUV and IR fields [16, 17, 43]. To conclude, we point out that the observation of the aforementioned results should be attainable with the current experimental performance. We think that experimental measurements with strong lasers would be highly desirable in order to corroborate the rich structure of the PE angle-resolved spectra specially in the perpendicular region.

## Acknowledgments

Work supported by CONICET PIP0386 and PIP0513, PICT-2014-2363 and PICT 2016-0296 of ANPCyT (Argentina), the University of Cuyo (UNCuyo 06/C487) and the University of Buenos Aires (UBACyT 20020130100617BA).

## Appendix. Ionization times and transition matrix calculations

The ionization times  $t_s$  that fulfill equation (11) are calculated as the intersection of the horizontal lines

$$\beta_{\pm}(\mathbf{k}) \equiv -k_z \pm \sqrt{v_0^2 - k_{\perp}^2} \quad (25)$$

and the vector potential  $A_L(t)$ . In figure 9 we represent schematically how the ionization times  $t_s$  are determined for a fixed momentum  $\mathbf{k}$  with  $k_z > 0$  (negative  $k_z$  can be straightforwardly deduced). We can distinguish two different situations depending on whether there are (or not) any solutions with the negative branch of the square root. If  $-k_z - \sqrt{v_0^2 - k_{\perp}^2} = \beta_{-}(\mathbf{k}) < -A_{L0}$  the negative branch never reaches any value of  $A_L(t)$ , and then there are only two times in the  $j$ th-optical cycle, i.e.,  $t^{(j,1)}$  and  $t^{(j,2)}$ . This case, illustrated in figure 9(a), corresponds to the called *parallel-like* region. Under this condition, when  $\beta_{+}(\mathbf{k}) > 0$  the emission times remain in the first half of the optical cycle. As  $\beta_{+}(\mathbf{k})$  decreases to zero, the release time  $t^{(j,1)}$  goes to the beginning of the laser cycle whereas the late release time  $t^{(j,2)}$  goes to the middle of it (see figure 9(a)). Finally, when  $\beta_{+}(\mathbf{k}) < 0$ , the two ionization times move to the second half of the optical cycle. This transition produces a discontinuity in the PE spectra as the one discussed in [37]. On the other

hand, when  $\beta_{-}(\mathbf{k}) > -A_{L0}$  the negative branch intersects  $A_L(t)$  at times  $t^{(j,3)}$  and  $t^{(j,4)}$  and, thus, there are four ionization times per optical cycle (see figure 9(b)). This condition defines the *perpendicular-like* region. As before, the times  $t^{(j,1)}$  and  $t^{(j,2)}$  may be in the first or second half of the  $j$ th-cycle depending on the momentum value, whereas  $t^{(j,3)}$  and  $t^{(j,4)}$  are always in the second one.

The ionization times of different cycles are simply related to the first one through

$$t^{(j,\alpha)} = t^{(1,\alpha)} + (2\pi/\omega_L)(j - 1), \quad (26)$$

where  $j = 1, 2, \dots, N$  indicates the  $j$ th optical cycle,  $N$  is the total number of laser cycles and  $\alpha = 1, 2, 3$  and 4 corresponds to the four ionization times per cycle described before. The solutions of equation (11) with  $\beta_{+}(\mathbf{k}) \geq 0$  lie in the first half cycle:

$$\begin{aligned} t^{(1,1)} &= \frac{1}{\omega_L} \sin^{-1} \left| \frac{\beta_{+}(\mathbf{k})}{A_{L0}} \right| \quad \text{and} \\ t^{(1,2)} &= \frac{\pi}{\omega_L} - t^{(1,1)}. \end{aligned} \quad (27)$$

Instead, if  $\beta_{+}(\mathbf{k}) < 0$ , they are in the second half cycle:

$$\begin{aligned} t^{(1,1)} &= \frac{\pi}{\omega_L} + \frac{1}{\omega_L} \sin^{-1} \left| \frac{\beta_{+}(\mathbf{k})}{A_{L0}} \right| \quad \text{and} \\ t^{(1,2)} &= \frac{3\pi}{\omega_L} - t^{(1,1)}. \end{aligned} \quad (28)$$

Furthermore, in the perpendicular-like region, the third and fourth ionization times are

$$\begin{aligned} t^{(1,3)} &= \frac{\pi}{\omega_L} + \frac{1}{\omega_L} \sin^{-1} \left| \frac{\beta_{-}(\mathbf{k})}{A_{L0}} \right| \quad \text{and} \\ t^{(1,4)} &= \frac{3\pi}{\omega_L} - t^{(1,3)}. \end{aligned} \quad (29)$$

In general, the ionization times depend on the starting time  $t_{xb}$  of the active window (see equation (22)). The previous analysis has been done for an IR laser whose vector potential vanishes at  $t_{xb}$ . When this is not the case, we have to consider a shift in the ionization times equations (27)–(29).

Finally, the transition matrix of equation (9) considering two or four ionization times per IR cycle in the parallel- or perpendicular-like situations results in

$$\begin{aligned} T_{if} &= \sum_{j=1}^N \left[ \sum_{\alpha=1}^2 g(\mathbf{k}, t^{(j,\alpha)}) + \Theta \left( 1 + \frac{\beta_{-}(\mathbf{k})}{A_{L0}} \right) \right. \\ &\quad \times \left. \sum_{\alpha=3}^4 g(\mathbf{k}, t^{(j,\alpha)}) \right], \end{aligned} \quad (30)$$

where we have introduced the Heaviside function  $\Theta$  so that the second term contributes only in the perpendicular-like case  $\beta_{-}(\mathbf{k}) \geq -A_{L0}$ . According to equation (9) the terms to



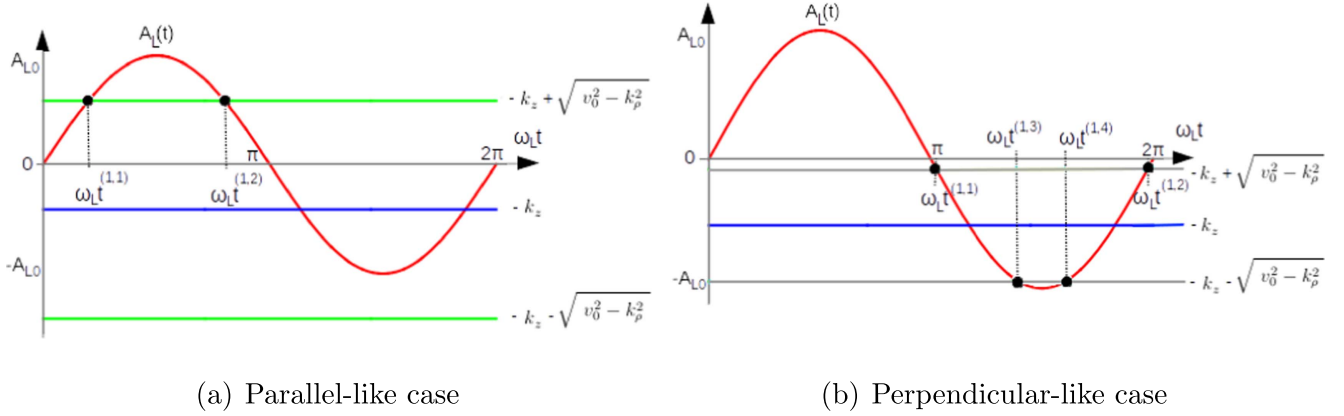


**Figure 9.** Emission times solutions of equation (11) as intersection of the three curves,  $A_L(t) = A_{L0} \sin(\omega_L t)$  in red solid line and the constants  $\beta_\pm = -k_z \pm \sqrt{v_0^2 - k_\perp^2}$  for a fixed electron momentum with  $k_z > 0$  and in the first IR oscillation cycle. In this scheme, the beginning time of the XUV pulse is zero. (a) Parallel-like case characterized by two ionization times per optical cycle. (b) Perpendicular-like case characterized by four ionization times per optical cycle.

add are

$$g(\mathbf{k}, t^{(j,\alpha)}) = \frac{\sqrt{2\pi} F_{X0}(t^{(j,\alpha)}) d_z(\mathbf{k} + \mathbf{A}_L(t^{(j,\alpha)}))}{|[\mathbf{k} + \mathbf{A}_L(t^{(j,\alpha)})] \cdot \mathbf{F}_L(t^{(j,\alpha)})|^{1/2}} \times \exp\left[iS(t^{(j,\alpha)}) + i\frac{\pi}{4} \text{sgn}[\dot{S}(t^{(j,\alpha)})]\right].$$

We note that the  $z$ -component of the dipole element (equation (10)) is proportional to  $k_z + A_L(t^{(j,\alpha)})$ , thus  $d_z$  evaluated in the first or second IR half cycle has equal magnitude and opposite sign. Therefore, we factorize  $|d_z|$  and introduce a minus sign ahead the Heaviside function in the second term of equation (30).

To evaluate action  $S$  (equation (8)) at the ionization es, let us consider the accumulated action  $\Delta S_{j\pm} = S(t^{(j,\alpha)}) - S(t^{(j,\alpha+1)})$  and the action average  $\bar{S}_{j\pm} = [S(t^{(j,\alpha)}) + S(t^{(j,\alpha+1)})]/2$  of two trajectories released in the same  $j$ th cycle, where the sign  $+$ ( $-$ ) corresponds to  $\alpha = 1(3)$  respectively. This results in  $\exp[iS(t^{(j,\alpha)})] = \exp(i\Delta S_{j\pm}/2 + i\bar{S}_{j\pm})$  and  $\exp[iS(t^{(j,\alpha+1)})] = \exp(-i\Delta S_{j\pm}/2 + i\bar{S}_{j\pm})$ . Replacing equations (26)–(29) into (8) we found that both accumulated actions are independent of the cycle  $j$ ,

$$\Delta S_\pm = \frac{\tilde{S}}{2} \left[ \frac{2}{\pi} \sin^{-1} |\beta_\pm(\mathbf{k})/A_{L0}| - 1 \right] - \frac{\text{sgn}[\beta_\pm(\mathbf{k})]}{2\omega_L} (4k_z + \beta_\pm(\mathbf{k})) \sqrt{A_{L0}^2 - \beta_\pm^2(\mathbf{k})} \quad (31)$$

and  $\bar{S}_{j\pm} = S_{0\pm} + j\tilde{S}$  depends linearly on the cycle index  $j$ , where  $\tilde{S} = (2\pi/\omega_L)(E + I_p + U_p - \omega_X)$  and  $S_{0-} = 3S_{0+} = -3\tilde{S}/4$ .

After a bit of algebra it can be shown that each of the  $N$  terms in equation (30) is proportional to

$$e^{ij\tilde{S}} \left[ f_+(\mathbf{k}) \cos\left(\frac{\Delta S_+}{2} + \frac{\pi}{4} \text{sgn}[\beta_+(\mathbf{k})]\right) - \Theta\left(1 + \frac{\beta_-}{A_{L0}}\right) f_-(\mathbf{k}) \cos\left(\frac{\Delta S_-}{2} - \frac{\pi}{4} \text{sgn}[\beta_-(\mathbf{k})]\right) \right],$$

where

$$f_\pm(\mathbf{k}) = e^{\pm i\tilde{S}/4} |1 - (\beta_\pm(\mathbf{k})/A_{L0})^2|^{-1/4}. \quad (32)$$

Finally, when the sum over the  $N$  optical cycles is achieved, the emission probability results in equation (14). The precedent results have been deduced for the  $k_z \geq 0$ . The negative cases, however, can be straightforwardly deduced replacing  $k_z$  by  $|k_z|$  in previous equations.

## ORCID iDs

A A Gramajo <https://orcid.org/0000-0001-8099-9245>  
R Della Picca <https://orcid.org/0000-0001-7909-4529>  
D G Arbó <https://orcid.org/0000-0002-4375-4940>

## References

- [1] Vénier V, Taïeb R and Maquet A 1995 *Phys. Rev. Lett.* **74** 4161–4
- [2] Schins J M, Breger P, Agostini P, Constantinescu R C, Muller H G, Bouhal A, Grillon G, Antonetti A and Mysyrowicz A 1996 *J. Opt. Soc. Am. B* **13** 197–200
- [3] Meyer M *et al* 2008 *Phys. Rev. Lett.* **101** 193002
- [4] Meyer M, Costello J T, Düsterer S, Li W B and Radcliffe P 2010 *J. Phys. B: At. Mol. Opt. Phys.* **43** 194006
- [5] Radcliffe P *et al* 2012 *New J. Phys.* **14** 043008
- [6] Mazza T *et al* 2014 *Nat. Commun.* **5** 3648
- [7] Hayden P *et al* 2016 *J. Mod. Opt.* **63** 358–66
- [8] Düsterer S *et al* 2016 *J. Phys. B: At. Mol. Opt. Phys.* **49** 165003
- [9] Drescher M and Krausz F 2005 *J. Phys. B: At. Mol. Opt. Phys.* **38** S727–40
- [10] Goulielmakis E *et al* 2004 *Science* **305** 1267–9
- [11] Johnsson P *et al* 2005 *Phys. Rev. Lett.* **95** 013001
- [12] Guyétand O *et al* 2005 *J. Phys. B: At. Mol. Opt. Phys.* **38** L357
- [13] Guyétand O *et al* 2008 *J. Phys. B: At. Mol. Opt. Phys.* **41** 051002
- [14] Bordas C, Noordam L D, Muller H G, van der Zande W J and Vrakking M J J 2004 *Phys. Scr.* **T112** 87

- [15] Meyer M *et al* 2012 *Phys. Rev. Lett.* **108** 063007
- [16] Düsterer S, Rading L, Johnsson P, Rouzée A, Hundertmark A, Vrakking M J J, Radcliffe P, Meyer M, Kazansky A K and Kabachnik N M 2013 *J. Phys. B: At. Mol. Opt. Phys.* **46** 164026
- [17] Picard Y J *et al* 2014 *Phys. Rev. A* **89** 031401
- [18] Itatani J, Quéré F, Yudin G L, Ivanov M Y, Krausz F and Corkum P B 2002 *Phys. Rev. Lett.* **88** 173903
- [19] Frühling U *et al* 2009 *Nat. Photon.* **3** 523–8
- [20] Wickenhauser M, Burgdörfer J, Krausz F and Drescher M 2006 *J. Mod. Opt.* **53** 247–57
- [21] Nagele S, Pazourek R, Feist J, Doblhoff-Dier K, Lemell C, Tokési K and Burgdörfer J 2011 *J. Phys. B: At. Mol. Opt. Phys.* **44** 081001
- [22] O’Keeffe P, López-Martens R, Mauritsson J, Johansson A, Johansson A, Vénard V, Taïeb R, Maquet A and Meyer M 2004 *Phys. Rev. A* **69** 051401
- [23] Glover T E, Schoenlein R W, Chin A H and Shank C V 1996 *Phys. Rev. Lett.* **76** 2468–71
- [24] Aseyev S A, Ni Y, Frasninski L J, Muller H G and Vrakking M J J 2003 *Phys. Rev. Lett.* **91** 223902
- [25] Swoboda M, Dahlström J M, Ruchon T, Johnsson P, Mauritsson J, L’Huillier A and Schafer K J 2009 *Laser Phys.* **19** 1591–9
- [26] Schins J M, Breger P, Agostini P, Constantinescu R C, Muller H G, Grillon G, Antonetti A and Mysyrowicz A 1994 *Phys. Rev. Lett.* **73** 2180–3
- [27] Kazansky A K and Kabachnik N M 2010 *J. Phys. B: At. Mol. Opt. Phys.* **43** 035601
- [28] Nandor M J, Walker M A, Van Woerkom L D and Muller H G 1999 *Phys. Rev. A* **60** R1771–4
- [29] Muller H G 1999 *Phys. Rev. A* **60** 1341–50
- [30] Kazansky A K, Sazhina I P and Kabachnik N M 2010 *Phys. Rev. A* **82** 033420
- [31] Bivona S, Bonanno G, Burlon R and Leone C 2010 *Laser Phys.* **20** 2036–44
- [32] Maquet A and Taïeb R 2007 *J. Mod. Opt.* **54** 1847–57
- [33] Jiménez-Galán A, Argenti L and Martín F 2013 *New J. Phys.* **15** 113009
- [34] Meyer M *et al* 2006 *Phys. Rev. A* **74** 011401
- [35] Taïeb R, Maquet A and Meyer M 2008 *J. Phys.: Conf. Ser.* **141** 012017
- [36] Kroll N M and Watson K M 1973 *Phys. Rev. A* **8** 804–9
- [37] Gramajo A A, Della Picca R, Garibotti C R and Arbó D G 2016 *Phys. Rev. A* **94** 053404
- [38] Gramajo A A, Della Picca R and Arbó D G 2017 *Phys. Rev. A* **96** 023414
- [39] Arbó D G, Ishikawa K L, Schiessl K, Persson E and Burgdörfer J 2010 *Phys. Rev. A* **81** 021403
- [40] Arbó D G, Ishikawa K L, Schiessl K, Persson E and Burgdörfer J 2010 *Phys. Rev. A* **82** 043426
- [41] Arbó D G, Ishikawa K L, Persson E and Burgdörfer J 2012 *Proc. 5th Int. Conf. on Elementary Processes in Atomic Systems Belgrade (Serbia, 21–25 June 2011); Nucl. Instrum. Methods Phys. Res. B* **279** 24–30
- [42] Haber L H, Doughty B and Leone S R 2009 *J. Phys. Chem. A* **113** 13152–8
- [43] Haber L H, Doughty B and Leone S R 2010 *Mol. Phys.* **108** 1241–51
- [44] Tong X M and Chu S I 1997 *Chem. Phys.* **217** 119–30
- [45] Tong X M and Chu S I 2000 *Phys. Rev. A* **61** 031401
- [46] Tong X M and Lin C D 2005 *J. Phys. B: At. Mol. Opt. Phys.* **38** 2593
- [47] Schöller O, Briggs J S and Dreizler R M 1986 *J. Phys. B: At. Mol. Phys.* **19** 2505
- [48] Messiah A 1965 *Quantum Mechanics I* (New York: North-Holland)
- [49] Dionissopoulou S, Mercouris T, Lyras A and Nicolaides C A 1997 *Phys. Rev. A* **55** 4397–406
- [50] Della Picca R, Fiol J and Fainstein P D 2013 *J. Phys. B: At. Mol. Opt. Phys.* **46** 175603
- [51] Macri P A, Miraglia J E and Gravielle M S 2003 *J. Opt. Soc. Am. B* **20** 1801–6
- [52] Wolkow D M 1935 *Z. Phys.* **94** 250–60
- [53] Chirilă C C and Potvliege R M 2005 *Phys. Rev. A* **71** 021402
- [54] Corkum P B, Burnett N H and Ivanov M Y 1994 *Opt. Lett.* **19** 1870–2
- [55] Ivanov M, Corkum P B, Zuo T and Bandrauk A 1995 *Phys. Rev. Lett.* **74** 2933–6
- [56] Lewenstein M, Kulander K C, Schafer K J and Bucksbaum P H 1995 *Phys. Rev. A* **51** 1495–507
- [57] Arbó D G, Miraglia J E, Gravielle M S, Schiessl K, Persson E and Burgdörfer J 2008 *Phys. Rev.* **77** 013401
- [58] Arbó D G, Yoshida S, Persson E, Dimitriou K I and Burgdörfer J 2006 *Phys. Rev. Lett.* **96** 143003
- [59] Arbó D G 2014 *J. Phys. B: At. Mol. Opt. Phys.* **47** 204008
- [60] Meyer M *et al* 2006 *Phys. Rev. A* **74** 011401
- [61] Meyer M *et al* 2008 *Phys. Rev. Lett.* **101** 193002
- [62] Meyer M 2010 *J. Phys.: Conf. Ser.* **212** 012018
- [63] Düsterer S *et al* 2016 *J. Phys. B: At. Mol. Opt. Phys.* **49** 165003
- [64] Della Picca R and Lindroth E 2015 *J. Phys. B: At. Mol. Opt. Phys.* **48** 245202
- [65] Boll D I R and Fojón O A 2014 *Phys. Rev. A* **90** 053414
- [66] Boll D I R and Fojón O A 2017 *J. Phys. B: At. Mol. Opt. Phys.* **50** 235604
- [67] Kazansky A K, Grigorieva A V and Kabachnik N M 2012 *Phys. Rev. A* **85** 053409
- [68] Kazansky A K, Bozhevolnov A V, Sazhina I P and Kabachnik N M 2014 *J. Phys. B: At. Mol. Opt. Phys.* **47** 065602